Enhanced three-dimensional deconvolution microscopy using a measured depth-varying point-spread function

Joshua W. Shaevitz[1,3,*] and Daniel A. Fletcher[2,4]

[1]*Department of Integrative Biology, University of California, Berkeley, California 94720, USA*
[2]*Department of Bioengineering, University of California, Berkeley, California 94720, USA*
[3]*Department of Physics, Princeton University, Princeton, New Jersey 08544, USA*
[4]*E-mail: fletch@berkeley.edu*
[*]*Corresponding author: shaevitz@princeton.edu*

Received February 26, 2007; revised April 23, 2007; accepted May 1, 2007;
posted May 3, 2007 (Doc. ID 80413); published July 27, 2007

We present a technique to systematically measure the change in the blurring function of an optical microscope with distance between the source and the coverglass (the depth) and demonstrate its utility in three-dimensional (3D) deconvolution. By controlling the axial positions of the microscope stage and an optically trapped bead independently, we can record the 3D blurring function at different depths. We find that the peak intensity collected from a single bead decreases with depth and that the width of the axial, but not the lateral, profile increases with depth. We present simple convolution and deconvolution algorithms that use the full depth-varying point-spread functions and use these to demonstrate a reduction of elongation artifacts in a reconstructed image of a 2 μm sphere. © 2007 Optical Society of America

OCIS codes: 100.3020, 100.6890, 110.0180, 140.7010, 170.6900, 180.2520.

1. INTRODUCTION

Three-dimensional (3D) deconvolution microscopy is a powerful tool for visualizing complex biological structures. This technique enhances resolution and contrast by using prior knowledge of a microscope's imaging response to estimate the underlying spatial pattern of fluorescent dye that gave rise to a measured image [1]. Practically, the blurring function can either be measured experimentally using sub-diffraction-sized fluorescent particles or calculated using a theoretical representation of the microscope's image forming optics [2].

The blurring function of a point source of a microscope's imaging optics is, in general, a function of the 3D position of the source in the sample plane. Theoretically, the point-spread function, or PSF, describes the blurring function of a linear and shift invariant (LSI) imaging system [3]. However, in the microscopy literature it has become common to use PSF to describe a microscope's blurring function [4], and we use the term PSF to refer to a single 3D blurring function for a microscope. In this paper, we address the change in the blurring function with depth below a coverglass, and term this response the depth-varying (DV) point-spread function (DVPSF).

Experimentally measured PSFs often yield the most accurate results due to subtleties in the optical system that are not captured by an idealized theoretical calculation. Specifically, aberrations induced by the objective lens or other elements in the imaging path are not captured by such parameters as the light wavelength, magnification, and numerical aperture of the imaging lens and the index of refraction of the material being probed. For example, spherical aberrations that result from the refractive index mismatch between the objective lens and coupling oil can be severe [5,6], especially in systems using high-numerical apertures. Also, the PSF has been measured to vary significantly with coverslip thickness and the refractive index of the sample [7]. These are just some of the complexities that make theoretical generation of the PSF difficult to achieve accurately. For the past half century, a large effort has been undertaken to correct for spherical and other aberrations optically [8–13]. Modern techniques using absorbing [6] or adaptive optics [14–16] have been successfully used to reduce many of these effects. However, a perfect, aberration-free imaging system has yet to be demonstrated.

Three-dimensional image deconvolution from a stack of two-dimensional (2D) images is further complicated by several factors. First, axial movement of the sample stage influences the position of the focal plane within the sample because of the index of refraction mismatch between the objective coupling medium, usually oil $n \sim 1.5$, and the sample medium, water for biological samples $n \sim 1.3$. This effect, termed the focal shift, can result in an axial image elongation of up to two times if not corrected. Corrections for the focal shift have been calculated theoretically and measured experimentally [17–26].

Second, the amount of light collected from a point source decreases with depth because of an axial broadening of the PSF. This is predicted by theoretical calculations that take into account spherical aberrations and the refractive index mismatch at the specimen interface [19,27,28] and has been measured using subresolution beads either embedded in an optical cement [7] or fixed to a tilted surface [18]. However, both of these measure-

ments use beads placed at random depths to measure this effect. Because the depth is not changed systematically in these experiments, one must interpolate between the measured PSFs to use them for 3D deconvolution [29]. Additionally, the index of an optical cement may not match the index of the final sample to be measured, and the use of different beads at each step may introduce bead–bead variation into the measured response. Motivated by these findings and their potential to reduce 3D deconvolution artifacts, we sought to design a system in which the DVPSF could be measured systematically and quickly with a single bead in any liquid medium.

2. MATERIALS AND METHODS

Our optical-trapping fluorescence microscope (Fig. 1) is a Nikon TE2000 equipped with epifluroescence imaging and modified to accept a 1064 nm laser (Spectra-Physics). Optical traps are convenient tools for manipulating the 3D position of sub-micrometer-sized objects [30,31]. Stable trapping of small fluorescent beads has been shown previously [32–34]. For all measurements reported here the trapping laser output was 300 mW. Axial steering of the laser focus was achieved using a motorized micrometer (Thorlabs) attached to a three-axis translation stage. Laser deflection signals were recorded using a position-sensitive detector (PSD) (Pacific Silicon Sensors) mounted in a plane conjugate to the back aperture of the condenser lens (Fig. 1, L3, PSD). PSD signals were amplified using custom electronics, antialias filtered, and recorded using a peripheral component interconnect (PCI)-based data acquisition card (National Instruments). The

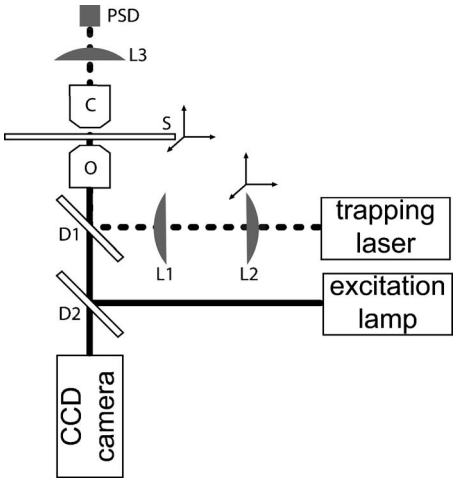

Fig. 1. Schematic of the optical-trapping deconvolution microscope. Excitation light from a xenon light source is coupled into the microscope via dichroic mirror D2, which reflects the excitation light but transmits the fluorescence emission wavelengths. The optical-trapping laser is injected via dichroic mirror D1, which reflects the IR laser but transmits visible wavelengths. Lenses L1 and L2 are set up in a one-to-one telescope such that L1 images the back aperture of the objective onto L2. Lens L2 is mounted on a three-axis stage with a motorized control along the optical axis, which allows for 3D steering of the optical trap in the object plane (see Section 3). The trapping light is transmitted through the objective and condenser lenses (O, C) and projected onto a position-sensitive detector imaged in the back-aperture of the condenser by lens L3. The specimen is mounted to a three-axis nanopositioning piezo stage (S).

specimen, contained in a flow cell made from a glass slide and coverslip separated by double-stick tape, was mounted on a computer-controlled, three-axis piezo stage with subnanometer positioning accuracy over a 100 μm $\times$100 μm$\times$20 μm range (Physik Instrumente). It is worth noting that the same aberrations that affect the blurring function for imaging also degrade the trapping laser focus, causing a reduction in trapping efficiency [35].

Images were recorded with a charge-coupled device (CCD) camera (QImaging) with 1392$\times$1040 pixels with physical dimensions of 6.45 μm$\times$6.45 μm. We used an infinity-corrected Apo total internal reflection fluorescence (TIRF) 100$\times$/1.49 NA oil-immersion objective lens with a 5$\times$ projection lens. By binning the camera acquisition by a factor of 2 in both lateral dimensions, we achieve an effective pixel size of 42 nm$\times$42 nm within the recorded image. Data acquisition and instrument control was implemented in LABVIEW (National Instruments), and all analysis was performed using custom software written in IGOR PRO (Wavemetrics) and the C programming language. Fourier transforms were implemented using the FFTW subroutine library [36].

We quantified the focal shift in our optical system by measuring the interference between the forward-scattered laser light and the light reflected between the trapped bead and planar coverglass surface as described by Neuman *et al.* [22]. Our measured focal shift of 0.71 agrees well with calculations from a purely theoretical model that incorporates diffraction at the interface [17] and yields a value of 0.75 for both the optical trapping wavelength of 1064 nm and the imaging wavelength of 532 nm. Our measurement is complicated by a decrease in the axial trap stiffness with depth [22]. However, we estimate that this correction is less than 3% by measuring the apparent change in the calculated focal shift as a function of depth and by directly measuring the trap stiffness at different depths. Furthermore, the lack of any PSF width increases with depth in the lateral direction (see Section 4) implies that the focal shift in our measurement of the DVPSF is not changing with depth and is approximately the same for the visible and IR light.

We used 170 nm Dragon Green fluorescent calibration beads (Bangs Labs) for the PSF recordings. These beads are of the order of the lateral diffraction-limited size of the imaging system of ~180 nm, and as such only approximate point sources. We chose these beads for our initial measurements as a trade-off between their reconstructed image size and their trapping efficiency, which scales as r^{-3}. Smaller beads require significantly more laser power to trap than the laser output used here and are difficult to detect with the PSD. Furthermore, it is formally possible to deconvolve the measured PSFs assuming a perfect 170 nm spherical source to achieve the true point-blurring function for applications in which the highest possible resolution is required. Here, we focus on demonstrating a reduction of deconvolution artifacts and do not perform this extra step.

To demonstrate the use of deconvolution with our DVPSF, we used 1.90$\pm$0.08 μm diameter YG fluorescent beads (Polysciences) adhered to the surface of a coverslip. To reduce the effect of readout noise in the reconstructions, we preconditioned the measured PSFs by thresh-

olding them such that all pixels at or below 3% of the maximum measured intensity were set to zero. Because our DVPSF only contains blurring functions for positions above the surface, i.e., within the sample, we apply the restoration algorithm only to parts of the image that lie above the surface. In our experiments we use the optical trap to measure the position of the surface relative to the objective focal plane to within approximately 20 nm [37]. This procedure yields surface positions that are confirmed by imaging small imperfections on the coverslip surface with differential interference contrast (DIC) microscopy.

3. MEASUREMENT OF THE DVPSF

By placing one lens of a one-to-one telescope from the laser-beam path in a plane conjugate to the back focal plane of the objective (Fig. 1, L2) we can steer the optical trap in 3D within the object space [31]. Briefly, moving the lens along the microscope optical axis changes the collimation of the laser, which shifts the z position of the laser focus, and hence the trap position, relative to the focal plane of the objective. By moving the piezodriven specimen stage and the optical trap axially, we can control both the axial trap position and the bead–surface separation independently.

We calibrated the imaging system and trap steering using the piezo-driven sample stage, which is calibrated against a National Institute of Standards and Technology (NIST)-traceable standard. By moving a surface-fixed bead laterally we measured the effective size of the CCD pixels to be 42 nm $\times$ 42 nm within the image. The stage was also used to calibrate the axial movement of the trap in the object space. We moved the stage a known amount and then measured the change in the position of the lens for which a trapped bead came into contact with the coverglass. We found that a millimeter of lens motion moved the optical trap 500 nm axially.

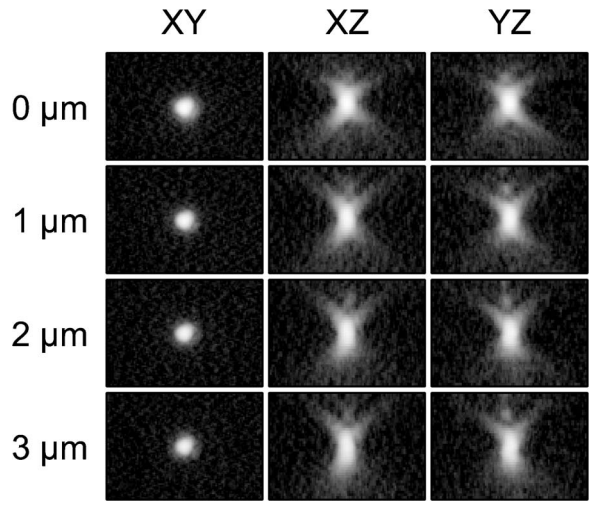

Fig. 2. Variation in the PSF with depth. Lateral and axial medial sections of an optically trapped 170 nm bead are shown at four different depths relative to the coverglass. Images are 4.2 μm $\times$ 2.8 μm. Images have been corrected for the measured focal shift before display. A logarithmic scale (Section 4) was used to enhance visualization of the low-amplitude regions of the image.

The DVPSF was recorded using a single 170 nm fluorescent trapped calibration bead and the following procedure. To form a PSF we scanned the axial position of the bead relative to the objective focal plane in 100 nm steps and recorded the bead image at each location. To measure the change in the PSF with depth, we scanned the stage position in 100 nm steps from in contact with the bead to approximately 5 μm below the trapped bead for each bead position. Because we used the same step increment for the bead and stage movements, we can recombine these images into PSFs from each bead depth (Fig. 2). In total our procedure records 2000 images, which are then reconstructed into 50 PSF image stacks that are each 40 planes high. This procedure, which is fully automated by computer, takes approximately 3 min for a 75 ms camera exposure in each frame.

Even with careful alignment of the three-axis lens stage relative to the optical axis of the microscope, we measured the residual $X-Z$ and $Y-Z$ position cross talk to be 3.2% and 7.8%, respectively. This mixing results in a tilting of each 3D PSF within the full DVPSF because we use the lens to move the bead relative to the imaging focal plane. PSFs centered at each depth were therefore corrected for this cross talk by shifting successive z planes in a direction opposite the measured tilt before use with deconvolution.

4. FEATURES OF THE DVPSF

Our systematically measured DVPSF exhibits similar features to those reported previously. In overall shape, the PSF changes from a fairly symmetric axial shape, resembling an "X," to an asymmetric, upright "Y" shape (Fig. 2). PSF images are displayed using a nonlinear logarithm scaling, which enhances the low-amplitude portions of the image (α was set to 500, for a full description see McNally *et al.* [7], p. 1058). This change in shape has been observed in several previous measurements of beads placed at different depths [7].

Axial and lateral line profiles of the DVPSF (Fig. 3) reveal two main effects of changes in depth. First, the peak intensity of the PSF decreases with depth (Fig. 4). Over a distance of 3 μm we measure a decrease in the peak intensity of the PSF of more than 40%. A similar decrease was observed by Diaspro *et al.* [18] and is predicted by theory [19,27,28].

Second, we observe an increase in the width of the PSF in the axial, but not the lateral direction with depth (Figs. 3 and 5). This increase has been reported previously [18] and is predicted by theory [19,27,28,38]. The effect of this increase in axial width on 3D image reconstruction is clear; features deep within the sample will appear dimmer and more blurred. In these measurements the total amount of light collected from the bead does not appear to change with depth. The decrease in peak amplitude is coincident with an increase in the profile width, such that the total collected light remains essentially constant.

5. CONVOLUTION AND DECONVOLUTION ALGORITHMS

In this section we develop a simple DV convolution algorithm that takes advantage of the fact that our uniformly

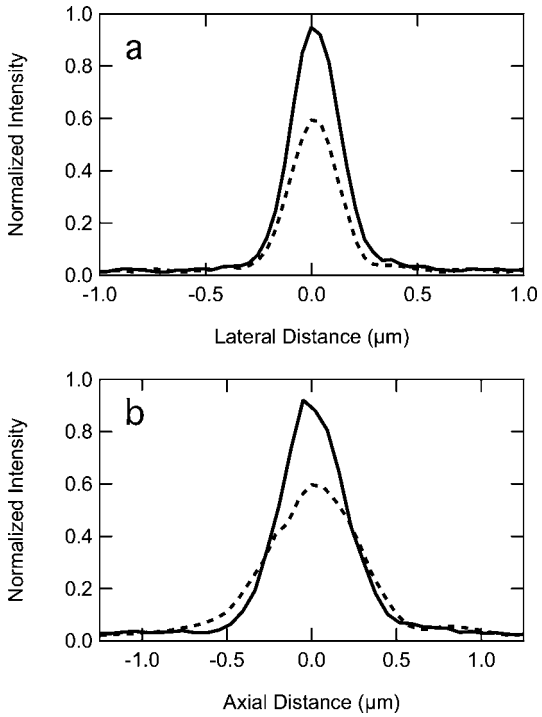

Fig. 3. Lateral and axial line profiles of the PSF at different depths. As the depth of the optically trapped bead is increased from 0 (solid curve) to 3 μm (dotted curve) the width of the central peak remains constant in a, the lateral dimensions but increases in b, the axial direction. The amplitude of the PSF scales with the axial width such that the total collected intensity at each depth remains constant.

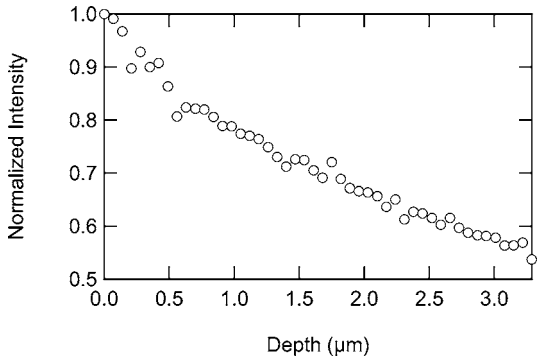

Fig. 4. Intensity of the PSF decreases with depth. The maximum measured intensity for a measured PSF is normalized by the value at the surface. The depth axis has been corrected for the measured focal shift.

spaced DVPSF includes a separate blurring function for each plane of intensity. We implement this convolution operation treating each plane of intensity separately and blurring it with the appropriate 3D PSF from the DVPSF set. The source image, $s(\mathbf{x}_o)$ where $\mathbf{x}_o=(x_0,y_0,z_0)$ is a 3D point in object space, can be written as the sum over the individual planes of intensity:

$$s(\mathbf{x}_o)=\sum_{z\in\mathcal{Z}} s_z(\mathbf{x}_o), \tag{1}$$

where

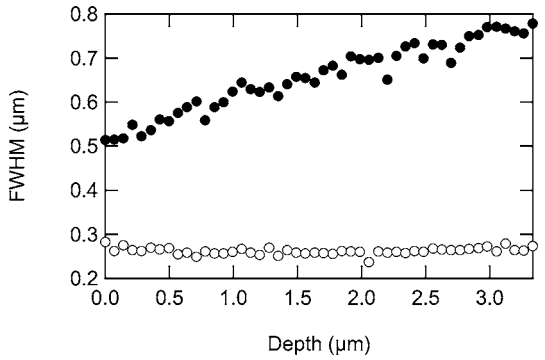

Fig. 5. Axial, but not lateral, PSF width increases with depth. The FWHM of the axial (solid circles) and lateral (open circles) line profiles of the measured PSFs is displayed. The depth axis has been corrected for the measured focal shift.

$$s_z(\mathbf{x}_o)=\begin{cases} s(\mathbf{x}_o) & \text{for } z_o=z \\ 0 & \text{otherwise} \end{cases}, \tag{2}$$

and $\mathcal{Z}$ is the set of all planes in the source image stack. The blurred image, $g(\mathbf{x}_i)$ where $\mathbf{x}_i$ is a 3D point in image space, can then be written as the sum of a series of 3D convolutions:

$$g(\mathbf{x}_i)=\sum_{z\in\mathcal{Z}}\left(\sum_{\mathbf{x}_o\in\mathcal{O}} h_z(\mathbf{x}_i-\mathbf{x}_o)s_z(\mathbf{x}_o)\right), \tag{3}$$

where $h_z(\mathbf{x})$ is the measured PSF centered at depth z as described in Section 3.

For deconvolution, we implemented Jansson's algorithm [39] for use with the convolution procedure described above. Jansson's algorithm constrains the restoration output to be positive gradually without forcing a truncation in the data, thus retaining information that truncating algorithms might lose [40]. For all reconstructions, we used a gain value of 2 [equivalent to the parameter b defined in Crilly [40], Eq. (7b)], and terminated the reconstruction when the percent change in the output image was less than 0.1% per iteration.

6. DECONVOLUTION OF A 2 μm SPHERE

Using our microscope we took a 3D image stack of a 1.9 μm fluorescent bead fixed to the coverglass. Figure 6a shows axial and lateral medial sections of the raw data. The raw fluorescence image appears elongated axially, being pointed on both the bottom and the top. Additionally, interference rings are present in both the axial and lateral sections.

Using this data and our measured DVPSF, we performed two different deconvolution procedures to compare our DV technique with more traditional non-depth-varying algorithms. Figure 6b shows the results of a deconvolution that ran for a total of 229 iterations using a single surface-bound PSF (3D) for all z planes. As has been noted previously [7], the top of the deconvolved bead image became pointed. Additionally, the interference rings are still present at low amplitudes, and the bright wings of intensity that extend diagonally from the bead remain, especially in the upper portion of the image.

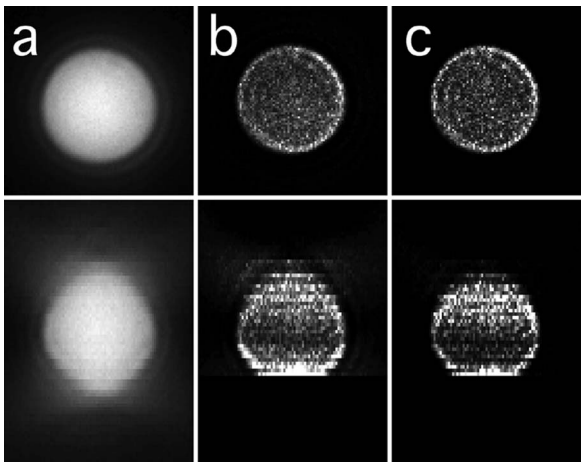

Fig. 6. Deconvolution of a 2 μm fluorescent sphere. Lateral (top row) and axial (bottom row) medial sections are displayed. Raw data from a, the wide-field fluorescence stack, and reconstructed images using b, the 3D and c, the DV deconvolution algorithms (see Section 6). Lateral sections are 3.8 μm $\times$ 3.8 μm. Axial sections are 3.8 μm $\times$ 5.3 μm. All images have been corrected for the measured focal shift before display.

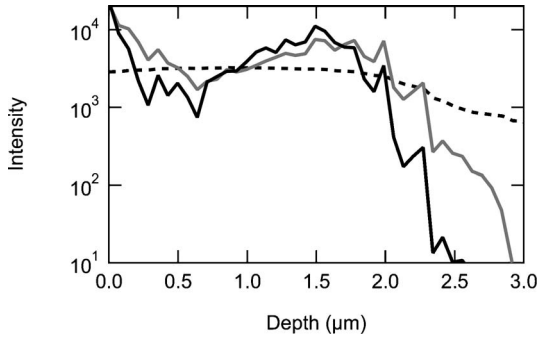

Fig. 7. Axial line profiles of the reconstructed fluorescent sphere images. The raw data (dotted curve), 3D deconvolution (gray curve) and DV deconvolution (solid black curve) are shown. Line profiles are an average of a 5×5 pixel beam extending axially through the center of each bead image.

Figure 6c shows the results of a deconvolution that ran for a total of 284 iterations using the full DVPSF. The DV deconvolution appears more spherical than the 3D deconvolution, lacking the pointed top to the bead image. The interference rings and bright wings have also been eliminated in the resultant image. This is especially apparent at larger depths, where the true PSF is very different from that measured at the surface, which is used in the 3D deconvolution.

The reduction in elongation artifacts is most easily seen in medial-axial line profiles through the middle of each reconstruction (Fig. 7). While the line profiles from the two methods are similar for depths less than 2 μm, the 3D deconvolution contains significant amplitude at depths up to $\sim$3 μm, whereas the DV line profile reaches an intensity count of 1 at 2.5 μm.

7. DISCUSSION

Using an optical trap we have developed a method for calibrating the full DVPSF of a wide-field fluorescence microscope. By independently controlling the axial position of the microscope sample and an optically trapped calibration bead, we are able to record changes to the PSF systematically with depth. We measure a change in axial symmetry and an axial broadening of the PSF in agreement with previous theoretical and experimental results. We further use this DVPSF to restore the 3D image of a 2 μm diameter bead, showing a reduction in deconvolution artifacts present in conventional reconstructions.

While our technique uses an optical trap to systematically localize the calibration bead, one could also use a bead physically attached to a probe such as an atomic force microscope (AFM) tip to achieve a similar result. However, unlike our purely optical approach, a physical probe will interact with both the excitation and emission light, making the interpretation of the measured DVPSF difficult. Another advantage of our all-optical system is that it is easily added onto any existing fluorescence microscope, wide-field or confocal, by introducing a single dichroic mirror (Fig. 1, D1) into the existing light path. Existing transoptical and epioptical paths can remain unmodified.

Furthermore, while we used an optical trap to measure the change in PSF with depth, one could also use translations of the optical trap to measure any lateral distortions in the blurring function. This, in principle, would allow the correction of all aberrations present in an image. However, the total amount of time, data, and computational power needed would probably be prohibitive.

In this work we used a fairly simple iterative algorithm to performing the DV image deconvolution for its ease of computation. Preza and Conchello [38] presented a stratum-based convolution model that takes into account a small number of PSFs for different depths and then interpolates between them. Using this algorithm they formulated an expectation–maximization (EM) algorithm to obtain pseudomaximum likelihood (ML) estimates (an EM–ML algorithm) for deconvolution assuming that the PSF is spatially varying weakly such that it is invariant over small regions, similar to algorithms developed for astronomical imaging [41,42]. However, while their algorithm can be used for a true DV deconvolution using a different PSF for each plane, EM–ML algorithms require many more iterations to reach convergence than simple algorithms such as the one used here. These algorithms typically require the square of the number of iterations needed for Jansson's algorithm. Additionally, Markham and Conchello [43] demonstrated that Jansson's algorithm typically yields reconstructions that are of similar quality to those from EM–ML reconstructions.

It is worth noting that our calibration technique requires the use of a high-power objective with large numerical aperture because of the requirements of a high gradient-to-scattering force ratio needed for stable optical trapping [31]. For very deep specimens, an alternative technique will have to be developed. However, for small biological specimens such as bacteria, our technique is uniquely suited for performing 3D image reconstructions for the purpose of localizing specific fluorescently labeled intracellular structures.

REFERENCES

1. D. Agard, Y. Hiraoka, P. Shaw, and J. Sedat, "Fluorescence

microscopy in three dimensions," Methods Cell Biol. **30**, 353–377 (1989).
2. S. Gibson and F. Lanni, "Experimental test of an analytical model of aberration in an oil-immersion objective lens used in three-dimensional light microscopy," J. Opt. Soc. Am. A **8**, 1601–1613 (1991).
3. J. Goodman, *Introduction to Fourier Optics* (Roberts & Co., 2004).
4. D. Agard, "Optical sectioning microscopy: cellular architecture in three dimensions," Annu. Rev. Biophys. Bioeng. **13**, 191–219 (1984).
5. B. Scalettar, J. Swedlow, J. Sedat, and D. Agard, "Dispersion, aberration and deconvolution in multi-wavelength fluorescence images," J. Microsc. **182**, 50–60 (1996).
6. I. Escobar, G. Saavedra, M. Martínez-Corral, and J. Lancis, "Reduction of the spherical aberration effect in high-numerical-aperture optical scanning instruments," J. Opt. Soc. Am. A **23**, 3150–3155 (2006).
7. J. McNally, C. Preza, J. Conchello, and L. Thomas, Jr., "Artifacts in computational optical-sectioning microscopy," J. Opt. Soc. Am. A **11**, 1056–1067 (1994).
8. J. Tsujiuchi, "Correction of optical images by compensation of aberrations and by spatial frequency filtering," Prog. Oceanogr. **2**, 133–180 (1963).
9. R. Barakat and A. Houston, "Transfer function of an annular aperture in the presence of spherical aberration," J. Opt. Soc. Am. **55**, 538–541 (1965).
10. J. Mills and B. Thompson, "Effect of aberrations and apodization on the performance of coherent optical systems. I. The amplitude impulse response," J. Opt. Soc. Am. A **3**, 694–703 (1986).
11. J. Ojeda-Castafieda, P. Andres, and A. Diaz, "Annular apodizers for low sensitivity to defocus and to spherical aberration," Opt. Lett. **11**, 487–489 (1986).
12. J. Ojeda-Castaneda, P. Andres, and A. Diaz, "Strehl ratio with low sensitivity to spherical aberration," J. Opt. Soc. Am. A **5**, 1233–1236 (1988).
13. S. Mezouari and A. Harvey, "Phase pupil functions for reduction of defocus and spherical aberrations," Opt. Lett. **28**, 771–773 (2003).
14. M. Booth, M. Neil, R. Juskaitis, and T. Wilson, "Adaptive aberration correction in a confocal microscope," Proc. Natl. Acad. Sci. U.S.A. **99**, 5788–5792 (2002).
15. E. Theofanidou, L. Wilson, W. Hossack, and J. Arlt, "Spherical aberration correction for optical tweezers," Opt. Commun. **236**, 145–150 (2004).
16. S. Somalingam, K. Dressbach, M. Hain, S. Stankovic, T. Tschudi, J. Knittel, and H. Richter, "Effective spherical aberration compensation by use of a nematic liquid-crystal device," Appl. Opt. **43**, 2722–2729 (2004).
17. S. Wiersma, P. Török, T. Visser, and P. Varga, "Comparison of different theories for focusing through a plane interface," J. Opt. Soc. Am. A **14**, 1482–1490 (1997).
18. A. Diaspro, F. Federici, and M. Robello, "Influence of refractive-index mismatch in high-resolution three-dimensional confocal microscopy," Appl. Opt. **41**, 685–690 (2002).
19. S. Hell, G. Reiner, C. Cremer, and E. Stelzer, "Aberrations in confocal fluorescence microscopy induced by mismatches in refractive index," J. Microsc. **169**, 391–405 (1993).
20. N. White, R. Errington, M. Fricker, and J. Wood, "Aberration control in quantitative imaging of botanical specimens by multidimensional fluorescence microscopy," J. Microsc. **181**, 99–116 (1996).
21. T. Visser, J. Oud, and G. Brakenhoff, "Refractive index and axial distance measurements in 3-d microscopy," Optik (Stuttgart) **90**, 17–19 (1992).
22. K. Neuman, E. Abbondanzieri, and S. Block, "Measurement of the effective focal shift in an optical trap," Opt. Lett. **30**, 1318–1320 (2005).
23. K. Carlsson, "The influence of specimen refractive index, detector signal integration, and non-uniform scan speed on the imaging properties in confocal microscopy," J. Microsc. **163**, 167–178 (1991).
24. H. Jacobsen and S. Hell, "Effect of the specimen refractive index on the imaging of a confocal fluorescence microscope employing high aperture oil immersion lenses," Bioimaging **3**, 39–47 (1995).
25. T. Visser, G. Brakenhoff, and F. Groen, "The one point response in fluorescence confocal microscopy," Optik (Stuttgart) **87**, 39–40 (1991).
26. T. Visser and J. Oud, "Volume measurements in three-dimensional microscopy," Scanning **16**, 198–200 (1994).
27. P. Török and P. Varga, "Electromagnetic diffraction of light focused through a stratified medium," Appl. Opt. **36**, 2305–2312 (1997).
28. C. Sheppard and P. Torok, "Effects of specimen refractive index on confocal imaging," J. Microsc. **185**, 366–374 (1997).
29. C. Preza and J. Conchello, "Image estimation accounting for point-spread function depth variation in three-dimensional fluorescence microscopy," in Proc. SPIE **4964**, 135–142 (2003).
30. A. Pralle, E. Florin, E. Stelzer, and J. Hoerber, "Photonic force microscopy: a new tool providing new methods to study membranes at the molecular level," Single Mol. **1**, 129–133 (2000).
31. K. Svoboda and S. M. Block, "Biological applications of optical forces," Annu. Rev. Biophys. Biomol. Struct. **23**, 247–285 (1994).
32. E. L. Florin, A. Pralle, J. K. Horber, and E. H. Stelzer, "Photonic force microscope based on optical tweezers and two-photon excitation for biological applications," J. Struct. Biol. **119**, 202–211 (1997).
33. F. Qian, "Combining optical tweezers and patch clamp for studies of cell membrane electromechanics," Rev. Sci. Instrum. **75**, 2937–2942 (2004).
34. A. Caspi, R. Granek, and M. Elbaum, "Diffusion and directed motion in cellular transport," Phys. Rev. E **66**, 011916 (2002).
35. A. Rohrbach and E. H. K. Stelzer, "Trapping forces, force constants, and potential depths for dielectric spheres in the presence of spherical aberrations," Appl. Opt. **41**, 2494–2507 (2002).
36. http://www.fftw.org/.
37. M. Lang, C. Asbury, J. Shaevitz, and S. Block, "An automated two-dimensional optical force clamp for single molecule studies," Biophys. J. **83**, 491–501 (2002).
38. C. Preza and J.-A. Conchello, "Depth-variant maximum-likelihood restoration for three-dimensional fluorescence microscopy." J. Opt. Soc. Am. A **21**, 1593–1601 (2004).
39. P. Jansson, *Deconvolution With Applications in Spectroscopy* (Academic, 1984).
40. P. Crilly, "A quantitative evaluation of various iterative deconvolution algorithms," IEEE Trans. Instrum. Meas. **40**, 558–562 (1991).
41. A. Boden, D. Redding, R. Hanisch, and J. Mo, "Massively parallel spatially-variant maximum likelihood restoration of Hubble Space Telescope imagery," J. Opt. Soc. Am. A **13**, 1537–1545 (1996).
42. M. Faisal, A. Lanterman, D. Snyder, and R. White, "Implementation of a modified Richardson–Lucy method for image restoration on a massively parallel computer to compensate for space-variant point spread function of a charge-coupled device camera," J. Opt. Soc. Am. A **12**, 2593–2603 (1995).
43. J. Markham and J. Conchello, "Fast maximum-likelihood image-restoration algorithms for three-dimensional fluorescence microscopy," J. Opt. Soc. Am. A **18**, 1062–1071 (2001).